

# Catalytic membrane nano reactor with Cu/ZnO *in situ* immobilized in membrane pores for methanol dehydrogenation

Yilin Wang<sup>1</sup>, Senqing Fan<sup>1</sup>, Zeyi Xiao<sup>1</sup>, Zenghui Mai<sup>1</sup>, Ke Bai<sup>1</sup>, Jiaojiao Chen<sup>1</sup>, Yu Chen<sup>1</sup>, and Jingyun Liu<sup>1</sup>

<sup>1</sup>Sichuan University

January 31, 2024

## Abstract

A catalytic membrane nano reactor (CMNR) with deep-permeation nanocomposite structure (DPNS) has been fabricated by flowing synthesis for methanol dehydrogenation to formaldehyde. In this structure, Cu/ZnO nanoparticles are *in situ* immobilized in the pores of Ti membrane substrate. The characterization by XRD, TGA, XPS, SEM and TEM indicates that the Cu/ZnO nanoparticles with mean size 82 nm was successfully embedded into the membrane pores, and well distributed along the thickness direction of the membrane. In the methanol dehydrogenation reaction, for one sheet of membrane setting up, the selectivity of formaldehyde 98%, the catalyst turnover frequency (*TOF*) 183 mmol·h<sup>-1</sup>·g<sup>-1</sup>, the pressure drop 2.7 kPa with gas permeating the membrane have been measured, under reaction temperature 360 , the gas flux 8 m<sup>3</sup>·m<sup>-2</sup>·h<sup>-1</sup> through the membrane.

## 1 Introduction

Formaldehyde is an important chemical intermediate and product<sup>1,2</sup>, and the production of formaldehyde by non-oxidative direct dehydrogenation of methanol has attracted widespread attention by academia and industry<sup>3,4</sup>. No greenhouse gas CO<sub>2</sub> is produced during the process of dehydrogenation of methanol with anhydrous formaldehyde obtained. In general, the fixed bed reactors with catalyst particles stacked randomly are used for dehydrogenation of methanol<sup>5</sup>. In this case, internal and external diffusion effects cannot be avoided at the scale of one catalyst particle owing to the limitation of mass transfer and heat transfer<sup>6</sup>, which can weaken the catalytic performance. Besides, the fluid channel between the catalyst particles is uneven due to a large number of particles stacked randomly, leading to the uneven flowing of the reactant across the catalyst particles. The uneven flowing in the catalytic bed will cause non-uniform distribution of residence time, temperature field and concentration field, which can further weaken the catalytic performance<sup>7,8</sup>. Especially, the local porosity of the catalytic bed is higher near the wall of the reactor and a channeling phenomenon is prone to existed<sup>9</sup>, which could make the non-uniform field distribution more serious. The non-uniform distribution of the field and the residence time would cause the formaldehyde converting into by-products such as CO, HCOOH, and HCOOCH<sub>3</sub><sup>4,10</sup>.

Membranes with micro or nano scale pores are good carriers for catalyst nanoparticles immobilization<sup>11</sup>. The catalytic membrane nano reactor (CMNR) with deep-permeation nanocomposite structure (DPNS) would be obtained if the nanoparticles are *in situ* immobilized in membrane pores along the thickness direction of the membrane. Multi-scale synergistic enhancement for catalysis can be achieved in CMNR during the subsequent dehydrogenation of methanol. (1) At the nanoparticles scale, the catalysts are immobilized in the membrane pores without being shaped. In this case, the reactant fluid can contact with all nanoparticles via flowing instead of diffusion<sup>12</sup>, which could increase the effective contact area between catalysts and reactant fluid, leading to the internal diffusion effect in conventional fixed bed reactors being eliminated. (2) At the scale of membrane pores, the catalytic reaction is confined within the membrane pores, which can reduce

the thickness of the mass transfer boundary layer<sup>13</sup>, improve the mass transfer efficiency, and eliminate the external diffusion effect in the conventional fixed bed reactor<sup>14</sup>. (3) At the scale of the catalytic bed layer, a sheet of membrane is designed as a catalytic bed layer, and good flowing uniformity can be achieved owing to the uniform disperse of the membrane pores. Therefore, the uniform distribution of residence time, concentration field and temperature field will be achieved<sup>15</sup>. Moreover, the multi catalytic bed layers can be set up in series with each layer controlled independently. Therefore, the precise control of temperature within the whole reactor can be achieved during the catalysis process.

In our previous study, it has been found that the catalytic nanoparticles can be *in situ* immobilized in membrane pores by flowing synthesis<sup>16-20</sup>. During this process, the precursor fluid for nanoparticles formation can permeate through the membrane pores under the external driven force. Several advantages can be realized by flowing synthesis (1) The catalytic nanoparticles can be immobilized in each membrane pore and distributed evenly along the thickness direction of the membrane. Under the external driven forces, the precursor fluid can overcome the surface tension of the liquid and flow in each membrane pores, which ensures the catalytic nanoparticles immobilized in each membrane pore; (2) Rapid mixing of the precursor and enhanced mass transfer and heat transfer can be achieved in the confined space of the membrane pores with micro or nano scale, which could promote the nanoparticles formation and structure regulation<sup>21</sup>; (3) According to the principle of deep filtration in porous media, the catalytic nanoparticles can be immobilized stably in tortuous membrane pores during flowing synthesis process under the effect of inertial force, Brownian motion and other factors.

In the field of methanol dehydrogenation, Cu and ZnO nanoparticles were performed high activity and remarkable selectivity to formaldehyde<sup>4,22-24</sup>. It has been reported that the yield of formaldehyde could be achieved at 60% under 650 with the catalysts containing Cu and Zn. In this work, porous Titanium membrane (Ti membrane) with good thermal conductivity, thermal stability and mechanical properties was used as the substrate. In order to increase the loading amount of Cu/ZnO nanoparticles immobilized in membrane pores, the Ti membrane substrate was firstly treated by heat alkali and silanization modified with amino groups grafted in membrane pores for metal ion chelation before Cu/ZnO nanoparticles immobilized. After that, the zeolitic imidazolate framework-8 (ZIF-8) was *in situ* immobilized in the treated Ti membrane substrate by flowing synthesis, then the Cu<sup>2+</sup> was introduced by ion-exchange between Cu<sup>2+</sup> and Zn<sup>2+</sup> in ZIF-8. Finally, Cu/ZnO nanoparticles were immobilized in the membrane pores by calcining and reducing to fabricate the Cu/ZnO/Ti CMNR. During the experiments of methanol dehydrogenation reaction, the effect of reaction temperature, reactant gas flux and the number of membranes setting up in series has been determined in CMNR.

## 2 Materials and methods

### 2.1 Materials

The porous Ti membrane substrate (wafer with diameter 20 mm, thickness 1 mm, pore size 10  $\mu\text{m}$ , and porosity 45%) was purchased from Kunshan Yinghuixiong electronic technology company; 3-aminopropyltriethoxysilane ( $\text{C}_9\text{H}_{23}\text{NO}_3\text{Si}$ ) was purchased from Macklin Biochemical company; 2-methylimidazole (2-mIm) was purchased from Aladdin (Shanghai); Methanol was purchased from Knowles; Zinc nitrate hexahydrate, copper nitrate trihydrate, ethanol, sodium hydroxide and acetone were all purchased from Chengdu Kelong company. All materials are analytical grade and were used as received without further purification.

### 2.2 Cu/ZnO/Ti CMNR fabricated by flowing synthesis

The Ti membrane substrate was washed with the acetone, ethanol and deionized water successively after being polished by the sand paper, in order to remove the burrs, scratches, oil stains and impurities. Then, the Ti membrane substrate was immersed in the sodium hydroxide solution ( $10 \text{ mol}\cdot\text{L}^{-1}$ ) at 80 for 2 h, followed with dried at 80 for 2 h. After that, the Ti membrane substrate was modified by 3-aminopropyltrimethoxysilane (APTES), followed with Cu/ZnO immobilization. A typical modification and assembly process was shown in Figure 1: (1) The mixed solution of 95 wt% ethanol and APTES ( $8 \text{ g}\cdot\text{L}^{-1}$ , 10 mL)<sup>25</sup> was permeating

through the Ti membrane substrate with the flowrate of  $5 \text{ mL}\cdot\text{h}^{-1}$ , then dried at  $80^\circ\text{C}$  for 2 h, so that the membrane was modified by APTES; (2) Zinc nitrate solution ( $0.845 \text{ mol}\cdot\text{L}^{-1}$ , 5 mL) was permeating through the Ti membrane substrate with the flowrate of  $1 \text{ mL}\cdot\text{h}^{-1}$ , followed with dried at  $80^\circ\text{C}$  for 2 h, so that  $\text{Zn}^{2+}$  was deposited in the pores of Ti membrane substrate; (3) 2-methylimidazole solution ( $2.151 \text{ mol}\cdot\text{L}^{-1}$ , 5 mL) was permeating through the membrane with the flowrate of  $1 \text{ mL}\cdot\text{h}^{-1}$ , and coordinated with the  $\text{Zn}^{2+}$  deposited in the pores of Ti membrane, and then, ZIF-8 was synthesized and immobilized in the pores after being dried at  $80^\circ\text{C}$  for 2 h; with repeating steps (2) and steps (3) several times, the loading amount of ZIF-8 could be increased effectively; (4) The ZIF-8/Ti membrane was washed with deionized water for several times to remove the unstable particles, and then dried at  $80^\circ\text{C}$  for 2 h; (5) The copper nitrate solution ( $0.053 \text{ mol}\cdot\text{L}^{-1}$ , 5 mL) was permeating through the ZIF-8/Ti membrane with the flowrate of  $1 \text{ mL}\cdot\text{h}^{-1}$ , and the  $\text{Cu}^{2+}$  was deposited stably and distributed uniformly in the membrane pores by ion-exchange between  $\text{Cu}^{2+}$  and  $\text{Zn}^{2+}$  in ZIF-8, followed with being dried at  $80^\circ\text{C}$  for 2 h to form  $\text{Cu}^{2+}/\text{Zn}^{2+}/\text{Ti}$  membrane; (6) The  $\text{Cu}^{2+}/\text{Zn}^{2+}/\text{Ti}$  membrane obtained in step (5) was washed with deionized water and dried at  $80^\circ\text{C}$  for 2 h to remove unstable particles; (7) Finally, the Cu/ZnO/Ti CMNR fabrication could be accomplished by reduced under 20%  $\text{H}_2/\text{N}_2$  environment at  $360^\circ\text{C}$  for 3 hours. During this process, ZIF-8 has been taken as a sacrificial intermediate. The above procedures from (1) to (6) were carried out *in situ* by means of the technological apparatus as shown in Figure S1, and the reduced and calcined procedure of (7) was achieved on the apparatus as shown in Figure S2.

For convenient comparison, the Cu/Ti membrane was fabricated without ZIF-8 as sacrificial intermediate, and the ZnO/Ti membrane was obtained by directly sintering the ZIF-8/Ti membrane under the air atmosphere as well.

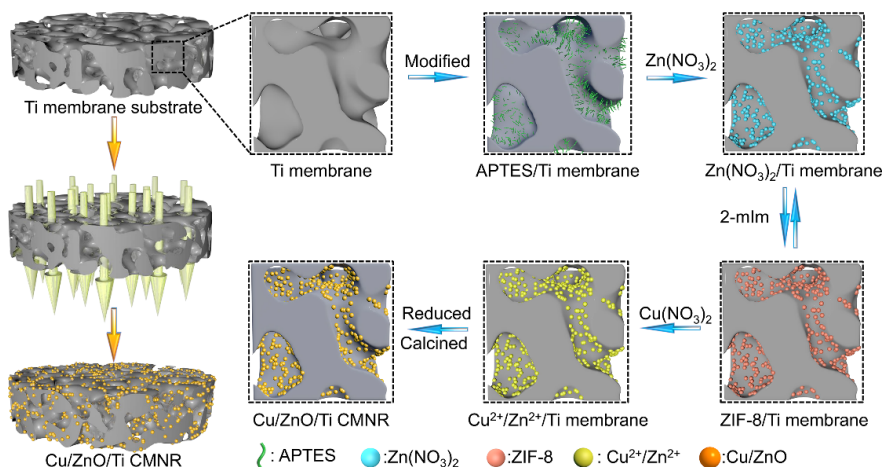


**FIGURE 1** Schematic diagram of fabricating CMNR by flowing synthesis

### 2.3 Experiments of methanol dehydrogenation reaction

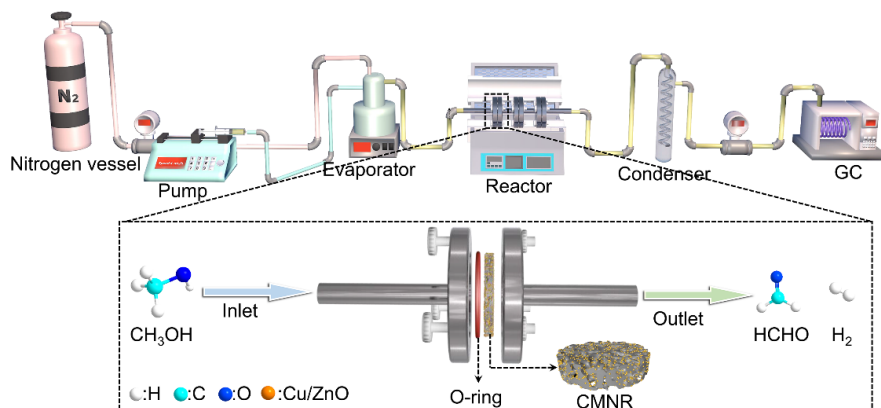


**FIGURE A:** schematic diagram of technological apparatus for catalytic dehydrogenation of methanol; **B:** membrane reactor setup

During the catalytic performance evaluation of the prepared CMNRs above, the following procedures were conducted: (1) The methanol liquid was pumped into the evaporator and evaporated at 120 ; (2) Methanol vapor was mixed with N<sub>2</sub> from nitrogen vessel in evaporator and the mixture reactant gas was flowed downward the reactor; (3) The mixture gas was permeated through the CMNR installed in the reactor and methanol in the mixture was cracked to form anhydrous formaldehyde, hydrogen and possible by-product under varied temperatures; (4) The product vapors were condensed in condenser, while the product gases were collected and detected by GC. On the apparatus, several reactors could be set up in serials, as shown in Figure S3.

## 2.4 Analysis methods

The microstructure and morphological characteristics of the membranes were observed by field emission scanning electron microscope (FESEM; JEOL, JSM700F) with ETD detector at 15 KV. The component and distribution of elements in the membranes were observed by the energy spectrum analysis system (EDS; Oxford instrument, INCA X-Max50). The X-ray diffraction (XRD) patterns were recorded by an EMPYREAN diffractometer with Cu ray at 40 kv, 40 mA to analyze the structure of crystal. The valence states of elements were detected on an X-ray photoelectron spectrometer (XPS; ESCALab220i-XL) with Al target ray, and the energy step was 1 eV. The thermogravimetric analysis was performed on a thermal analysis system (TGA; TGA/DSC2) in Ar, and the temperature was increased from 30 to 650 with the heating rate of 10 ·min<sup>-1</sup>. The field emission transmission electron microscope and high-resolution transmission electron microscope (TEM and HRTEM; FEI, Tecnai G22 F20 S-TWIN) were used to observe the morphology of nanoparticles that immobilized in the membrane pores. The TEM and HRTEM samples were prepared by cleaning the CMNRs in ultrasound for 24 h, and the suspension was centrifuged at 8000 r·min<sup>-1</sup> for 15 min. Finally, the powder was dispersed in methanol after being washed with methanol for 3 times. The loading amount of Cu and Zn in the CMNR were analyzed based on a plasma spectrometer (ICP; Agilent 725ES).

The liquid and gas products at the outlet of the CMNR were analyzed by gas chromatography workstation (GC-9790 II, Zhejiang Fuli). The liquid products were detected by flame ionization detector (FID) using an LZP-930 column (30 m × 0.32 μm × 1.0 μm), and the temperature of the injection was set at 180 , the temperature of column oven was set at 50 , the temperature of the detector was set at 180 . The carrier gas was nitrogen and its flowrate was 40 mL·min<sup>-1</sup>. The gas products were detected by thermal conductivity detector (TCD) using a TDX-01 column (2 m × 3 mm), and the temperature of the injection was set at 100 , the temperature of column oven was set at 90 , the temperature of the detector was set at 100 . The carrier gas was nitrogen and its flowrate was 24 mL\*min<sup>-1</sup>.

During the process of methanol dehydrogenation to formaldehyde in CMNR, the reaction equations can be described as follows according to the analyzed results of products (Figure S4):

Combining Eq. (1) and Eq. (2), the productivity of formaldehyde ( $P_{FA}$ ,  $\text{mmol}\cdot\text{h}^{-1}\cdot\text{g}^{-1}$ ) could be described as follows:

The productivity of hydrogen ( $P_{H_2}$ ,  $\text{mmol}\cdot\text{h}^{-1}\cdot\text{g}^{-1}$ ) was calculated as:

where  $C_{H_2}$  was the volume fraction of hydrogen of the outlet, %;  $V_{gas}$  was the volume of gas that collected at the downward of the CMNR, mL;  $t$  was the reaction time, h;  $g_{cat}$  was the loading amount of Cu/ZnO nanoparticles immobilized in the CMNR, g.

The productivity of methyl formate ( $P_{MF}$ ,  $\text{mmol}\cdot\text{h}^{-1}\cdot\text{g}^{-1}$ ) was calculated as:

where  $C_{MF}$  was the mass concentration of MF in the condensate,  $\text{mg}\cdot\text{g}^{-1}$ ;  $m$  was the mass of the condensate, g;  $M_{MF}$  was the molecular weight of MF, which was  $60.05 \text{ g}\cdot\text{mol}^{-1}$ .

The conversion efficiency of methanol ( $X_{MeOH}$ , %) was calculated as:

where  $F_{MeOH}$  was the flowrate of methanol vapor that permeated into the CMNR,  $\text{mmol}\cdot\text{h}^{-1}$ .

The selectivity of the formaldehyde ( $S_{FA}$ , %) was calculated as:

The selectivity of the methyl formate ( $S_{MF}$ , %) was calculated as:

The catalyst turnover rate ( $TOF$ ,  $\text{mmol}\cdot\text{h}^{-1}\cdot\text{g}^{-1}$ ) was calculated as:

The formaldehyde production capacity was defined as the production of per membrane thickness of CMNR ( $Y_{FA}$ ,  $\text{mmol}\cdot\text{h}^{-1}\cdot\text{mm}^{-1}$ ) and it could be calculated as:

where  $\delta$  was the thickness of CMNR, mm.

The hydrogen production capacity was defined as the production of per membrane thickness of CMNR ( $Y_H$ ,  $\text{mmol}\cdot\text{h}^{-1}\cdot\text{mm}^{-1}$ ) and it could be calculated as:

The gas permeability and the pressure drop of the CMNR was measured on an apparatus shown in Figure S5. And the permeability ( $\text{m}^3\cdot\text{m}^{-2}\cdot\text{h}^{-1}\cdot\text{kPa}^{-1}$ ) can be calculated as:

where  $F$  was the flowrate of nitrogen,  $\text{m}^3\cdot\text{h}^{-1}$ ;  $\Delta P$  was the pressure drop of the transmembrane, kPa;  $A$  was the effective area of the CMNR,  $3.14 \text{ cm}^2$ .

The reactant gas flux through the membrane  $J(\text{m}^3\cdot\text{m}^{-2}\cdot\text{h}^{-1})$  can be calculated as:

where  $V$  was the volume of reactant gas,  $\text{m}^3$ .

### 3 Results and discussion

#### 3.1 Characterization of the CMNR

##### 3.1.1 Structure of the CMNR

The X-ray diffraction patterns of Ti membrane substrate, ZIF-8/Ti membrane,  $\text{Cu}^{2+}/\text{Zn}^{2+}/\text{Ti}$  membrane and Cu/ZnO/Ti CMNR were shown in Figure 3. For the Ti membrane substrate, the diffraction peaks appeared at  $2\theta=35.1^\circ$ ,  $38.4^\circ$ ,  $40.2^\circ$ ,  $53.0^\circ$ ,  $62.9^\circ$ ,  $70.7^\circ$ ,  $76.2^\circ$  and  $77.4^\circ$  were corresponded to the (100), (002), (101), (102), (110), (103), (112) and (201) crystal planes of Ti. After assembly of ZIF-8 nanoparticles in Ti membrane, new diffraction peaks appeared at  $2\theta=7.3^\circ$ ,  $10.4^\circ$ ,  $12.7^\circ$ ,  $14.7^\circ$ ,  $16.5^\circ$  and  $18.0^\circ$  were corresponded to ZIF-8. In addition to the diffraction peaks of ZIF-8, there were some miscellaneous peaks, which may be attributed to the insufficient purity of the prepared ZIF-8 nanoparticles and the binding or covering of Zn sites on ZIF-8 by APTES<sup>26</sup>. Part of the diffraction peaks of the ZIF-8 crystal were weakened or even disappeared with the collapse of ZIF-8 structure, after the  $\text{Cu}(\text{NO}_3)_2$  solution permeated through the ZIF-8/Ti membrane, since the  $\text{Cu}^{2+}$  and  $\text{Zn}^{2+}$  were similar in atomic radii and the coordination binding force of  $\text{Cu}^{2+}$  and 2-mIm was stronger than that of  $\text{Zn}^{2+}$ , leading to  $\text{Zn}^{2+}$  in ZIF-8 replaced by  $\text{Cu}^{2+}$ <sup>17,27-30</sup>. For the Cu/ZnO/Ti CMNR, the diffraction peaks at  $2\theta=31.7^\circ$ ,  $34.3^\circ$ ,  $36.3^\circ$ ,  $47.3^\circ$ ,  $56.6^\circ$ ,  $67.9^\circ$  and  $69.1^\circ$  were corresponded to the (100), (002), (101), (102), (110), (112) and (201) crystal planes of ZnO and the

diffraction peaks at  $2\theta=43.3^\circ$  and  $50.4^\circ$  that could be corresponded to the (111) and (200) crystal planes of  $\text{Cu}^0$  were also appeared in the  $\text{Cu}/\text{ZnO}/\text{Ti}$  CMNR. This phenomenon implied that the  $\text{Cu}/\text{ZnO}$  nanoparticles were successfully immobilized in the Ti membrane substrate by flowing synthesis. The ZnO in  $\text{Cu}/\text{ZnO}/\text{Ti}$  CMNR should be derived from  $\text{Zn}(\text{NO}_3)_2$  during the process of ion exchange between  $\text{Cu}^{2+}$  of  $\text{Cu}(\text{NO}_3)_2$  and  $\text{Zn}^{2+}$  of ZIF-8, since ZIF-8 can only be thermally decomposed into ZnO in air atmosphere instead of nitrogen atmosphere, but  $\text{Zn}(\text{NO}_3)_2$  could be thermally decomposed into ZnO in nitrogen atmosphere, as shown in Figure S6. In addition, the diffraction peaks of oxidized Cu were also found in the  $\text{Cu}/\text{ZnO}/\text{Ti}$  CMNR, which might be owing to partial oxidation of Cu by oxygen in the air.

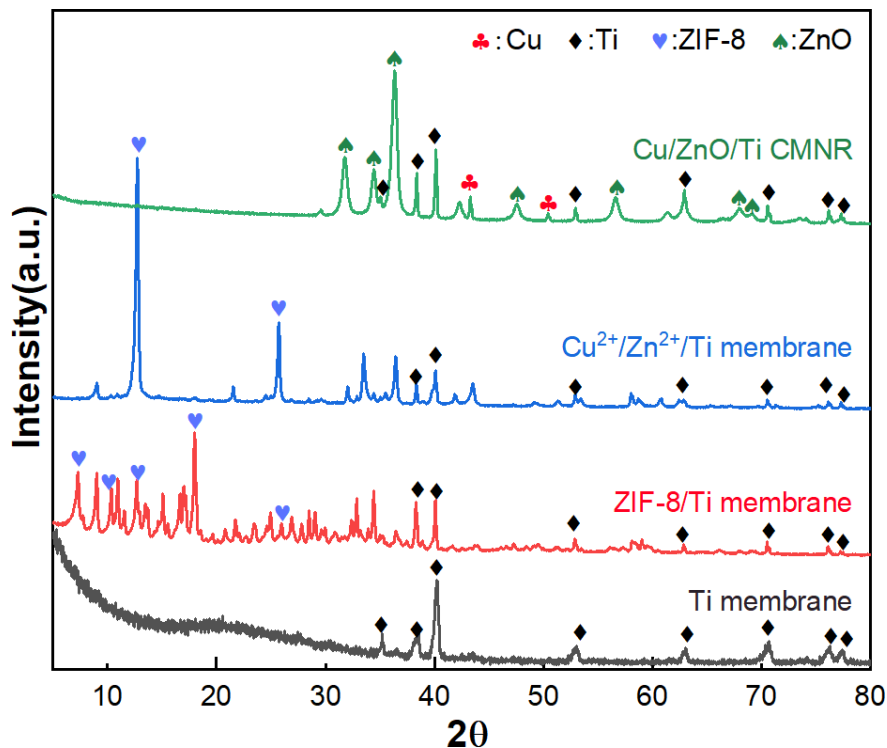


**FIGURE 3** XRD patterns of Ti membrane substrate, ZIF-8/Ti membrane,  $\text{Cu}^{2+}/\text{Zn}^{2+}/\text{Ti}$  membrane and  $\text{Cu}/\text{ZnO}/\text{Ti}$  CMNR

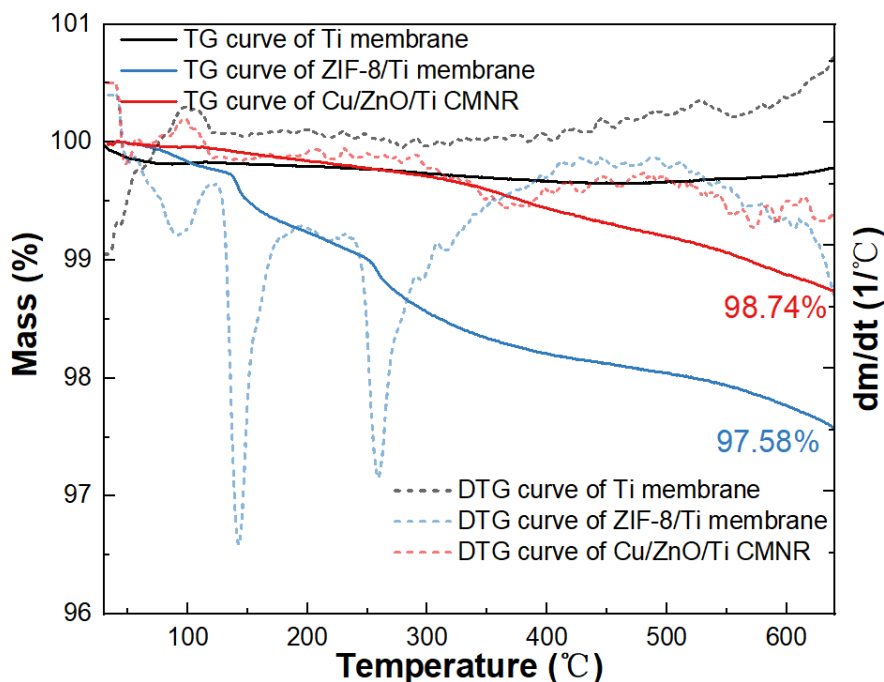


**FIGURE 4** TG and DTG curves of Ti membrane substrate, ZIF-8/Ti membrane and Cu/ZnO/Ti CMNR

The TG and DTG curves of Ti membrane substrate, ZIF-8/Ti membrane and Cu/ZnO/Ti CMNR were shown in Figure 4. It was found that the mass of Ti membrane substrate was hardly changed in the range of 35 and 650 , which implied the good thermal stability of Ti membrane substrate. Two obvious mass degradation phenomena were observed in the two intervals of 100 ~150 and 250 ~400 for the ZIF-8/Ti membrane, as shown in the DTG curve. The two steps can be attributed to the decomposition of guest molecules (such as uncoordinated 2-mIm and solvent molecules) and the gradual collapse of ZIF-8, respectively. No significant step was observed in the TG curve of Cu/ZnO/Ti CMNR, which indicated the Cu/ZnO nanoparticles that immobilized in the pores of Ti membrane substrate having good thermal stability. A gradual mass decrease can be observed for ZIF-8/Ti membrane and Cu/ZnO/Ti CMNR from 400 ~650 , which could be due to the decomposition of organic matter after Ti membrane substrate was modified by silanization<sup>31</sup>. After being heated at 650 , the residual mass percentages were in the order: Ti membrane substrate > Cu/ZnO/Ti CMNR > ZIF-8/Ti membrane.

In order to analyze the elements and valence states of the nanoparticles immobilized in membrane, the Ti membrane substrate, ZIF-8/Ti membrane and Cu/ZnO/Ti CMNR were scanned by X-ray electrons, and the results were shown in Figure 5A. It can be seen that Ti element, O element due to the surface passivation and C element due to the carbon adsorption could be detected for Ti membrane substrate<sup>32</sup>. Zn and N elements were found for ZIF-8/Ti membrane in addition to C and O, which were the components of ZIF-8 exactly. For Cu/ZnO/Ti CMNR, the Cu, Zn, O, Ti and C elements were found without N element detected, which indicated the ZIF-8 was collapsed and the enhancement of O element peak intensity could ascribe to the Zn<sup>2+</sup> derived into ZnO. It should be noted that Ti element was disappeared in ZIF-8/Ti membrane and only a weak signal of Ti element was found in Cu/ZnO/Ti CMNR, which could be clearly observed from the high-resolution scan spectrum of Ti element (Figure 5B). The peaks at the binding energies of 464.5 eV and 458.65 eV were corresponded to the 2p<sub>1/2</sub> and 2p<sub>3/2</sub> orbitals of Ti<sup>4+</sup>, respectively. This indicated that the Ti element in Ti membrane substrate existed in the form of TiO<sub>2</sub>, which was contradict with XRD results. This contradiction phenomenon may owe to the difference in the detection depth between XRD and XPS scanning, since the XPS could only reach the TiO<sub>2</sub> film on the surface of Ti membrane substrate. Besides, the disappearance or weakness of Ti element in ZIF-8/Ti membrane and Cu/ZnO/Ti CMNR can be also

explained by the low detection depth of XPS, since the signal of Ti element from XPS was hidden due to ZIF-8 or Cu/ZnO immobilized in the pores of the Ti membrane substrate. The high-resolution scanning energy spectrums of Zn in ZIF-8/Ti membrane and Cu/ZnO/Ti CMNR were shown in Figure 5C. The characteristic peaks at 1044.6 eV and 1021.5 eV were corresponded to 2p<sub>1/2</sub> and 2p<sub>3/2</sub> orbital of Zn<sup>2+</sup>, indicating that the Zn element existed in ZIF-8/Ti membrane was in the form of a divalent ion. The valent state of Cu element in the Cu/ZnO/Ti CMNR could be identified in Figure 5D. Two characteristic peaks at 952.05 eV and 932.1 eV were attributed to 2p<sub>1/2</sub> and 2p<sub>3/2</sub> orbital of Cu<sup>0</sup>, which proved most of the Cu elements were existed in the form of zero valence in Ti membrane substrate. In addition, the characteristic peak at 934.5 eV could be corresponded to the 2p<sub>3/2</sub> orbital of Cu<sup>2+</sup>, indicating that a small amount of Cu element was oxidized by air, which was consistent with the results of XRD.

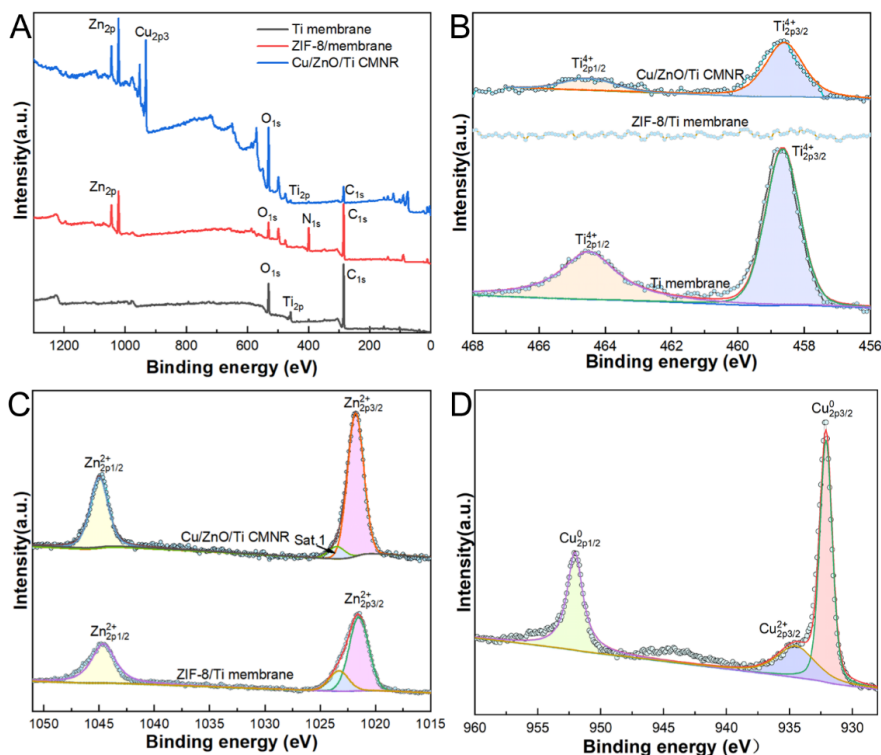


**FIGURE 5** XPS survey spectra of Ti membrane substrate, ZIF-8/Ti membrane and Cu/ZnO/Ti CMNR (A); High-resolution XPS spectra of Ti 2p (B), Zn 2p (C) and Cu 2p (D)

The loading amount of Cu and ZnO immobilized in Cu/Ti membrane, ZnO/Ti membrane and Cu/ZnO/Ti CMNR were analyzed by ICP and calculation, with the results shown in Table 1. The loading amount of Cu nanoparticles in Cu/Ti membrane was lower than 0.01 mg·g<sup>-1</sup> (Ti substrate) due to the inert and poor retention of Ti membrane substrate, if the Cu<sup>2+</sup> solution was directly permeated through Ti membrane substrate without ZIF-8 as carrier. Immobilizing ZIF-8 in Ti membrane substrate followed with calcined in air, over 21 mg of ZnO per gram of Ti substrate can be immobilized in membrane pores. Immobilizing ZIF-8 in Ti membrane substrate as a sacrificial intermediate followed with Cu<sup>2+</sup> ion exchange and reduction, the loading amount of Cu was about 13 times higher than that in Cu/Ti membrane without ZIF-8 immobilization in advance. Two key issues can be devoted to the loading increase of Cu after immobilization of ZIF-8. The pore size of Ti membrane substrate would be reduced, which can inhibit Cu nanoparticles leaching from the membrane pores during Cu nanoparticles immobilization in membrane pores. Besides, ZIF-8 with high specific area could adsorb Cu<sup>2+</sup> via ion-exchange<sup>27</sup>. High amount of Cu<sup>2+</sup> adsorption in membrane pores could increase the loading amount of Cu nanoparticles.

**TABLE 1** The loading amount of Cu and ZnO nanoparticles in Ti membrane by ICP test and calculation

Samples	Cu (mg·g <sup>-1</sup> )	ZnO (mg·g <sup>-1</sup> )	Cu/ZnO (mg·g <sup>-1</sup> )
Cu/Ti membrane	0.093	-	-
ZnO/Ti membrane	-	21.233	-
Cu/ZnO/Ti CMNR	1.232	23.127	24.359

### 3.1.2 Morphology of the CMNR

The morphologies of Ti membrane substrate, ZIF-8/Ti membrane and Cu/ZnO/Ti CMNR could be observed through Figure 6. The porous structure and smooth surface could be clearly observed for the Ti membrane substrate from Figure 6(A1, A2). The pores can be still observed after ZIF-8 and Cu/ZnO has been immobilized in membrane pores (Figure 6(B1, C1)). This phenomenon implied that the pores of the Ti membrane substrate cannot be blocked by the immobilization nanoparticles. And numerous nanoparticles could be observed in membrane pores (Figure 6(B1, B2)). Besides, the Ti membrane substrate, ZIF-8/Ti membrane and Cu/ZnO/Ti CMNR were cut off and the cross-sectional morphology characteristics were observed. It could be observed that there was no nanoparticle distributed in the pores of Ti membrane substrate and the sintered bulk metal piled up to form an open pore structure, as shown in Figure 6(A3). After the Zn<sup>2+</sup> solution and 2-mIm solution were permeated through the Ti membrane substrate in turn, the coordination reaction between Zn<sup>2+</sup> and 2-mIm resulted in the formation of a large amount of 2D flake-shaped ZIF-8<sup>33</sup> in the pores of Ti membrane substrate with the average particle size of ZIF-8 being 208 nm, as shown in Figure 6(B3) and Figure S7(A). The Cu<sup>2+</sup> solution was permeated through the ZIF-8/Ti membrane and then calcined at 360 under H<sub>2</sub>/N<sub>2</sub> environment and spherical Cu/ZnO nanoparticles were successfully immobilized in membrane pores with an average particle size of 82 nm, as shown in Figure 6(C3) and Figure S7(B). The TEM image of ZIF-8 nanoparticles in ZIF-8/Ti membrane was shown as Figure 6D, and the regular dodecahedron crystal of ZIF-8 can be clearly observed. The TEM and HRTEM images of Cu/ZnO nanoparticles in Cu/ZnO/Ti CMNR were shown as Figure 6E and Figure 6F, respectively. The distance of 0.260 nm and 0.181 nm belong to ZnO (002) crystal plane and Cu (200) crystal plane, which proved the Cu<sup>0</sup> and ZnO were immobilized in the membrane pores successfully by calcination and reduction.

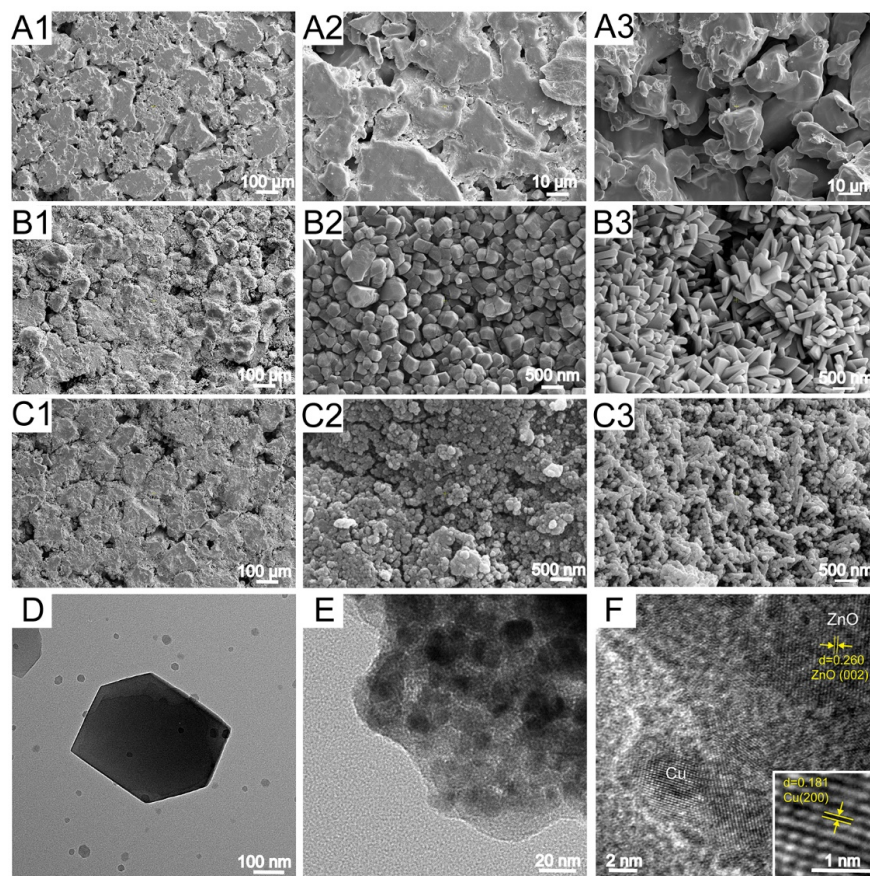


**FIGURE 6** FESEM images of surface morphologies of Ti membrane substrate (A1, A2), ZIF-8/Ti membrane (B1, B2) and Cu/ZnO/Ti CMNR (C1, C2); FESEM images of cross-sectional morphologies of Ti membrane substrate (A3), ZIF-8/Ti membrane (B3) and Cu/ZnO/Ti CMNR (C3); TEM images of ZIF-8 nanoparticles in ZIF-8/Ti membrane (D); TEM images (E) and HRTEM image of Cu/ZnO nanoparticles in Cu/ZnO/Ti CMNR.

The compositions of elements on the cross-section of ZIF-8/Ti membrane and Cu/ZnO/Ti CMNR were obtained by EDS, as shown in Figure S8. After ion-exchange and reduction, the atomic percentage of N in the membrane decreased from 5.15% to 0%, and the atomic percentage of O increased from 11.85% to 34.69%, which indicated the successful immobilization of ZnO in the pores of Ti membrane substrate. The element distribution of the whole cross-section of the Cu/ZnO/Ti CMNR was shown in Figure S9. It could be obviously found that Cu, Zn, and O elements were uniformly distributed along the cross-section, which proved that the Cu/ZnO nanoparticles can be successfully distributed along the thickness direction of the Ti membrane substrate by flowing synthesis.

### 3.1.3 Permeability of the CMNRs

The size of the membrane pores would be decreased after the nanoparticles immobilization in membrane pores, which could reduce the permeability of the membrane. The permeability of Ti membrane, ZIF-8/Ti membrane and Cu/ZnO/Ti CMNR were determined before the experiment of methanol dehydrogenation, in order to explore the effect of the nanoparticles immobilized in the pores of Ti membrane substrate on the permeability of the membrane. The results were shown in Figure 7. It can be seen that the Ti membrane substrate has the best permeability, which is  $105 \text{ m}^3 \cdot \text{m}^{-2} \cdot \text{h}^{-1} \cdot \text{kPa}^{-1}$ . The permeability of the membrane could be reduced significantly, if ZIF-8 nanoparticles were immobilized in membrane pores. It can be calculated

that the permeability of the ZIF-8/Ti membrane was only  $0.41 \text{ m}^3 \cdot \text{m}^{-2} \cdot \text{h}^{-1} \cdot \text{kPa}^{-1}$ , which was three orders of magnitude lower than that of Ti membrane substrate. The decrease of membrane pore size after ZIF-8 immobilization could lead to the increase of transmembrane resistance for gas permeating, resulting to the decrease permeability of membrane. Compared with ZIF-8/Ti membrane, the permeability of the Cu/ZnO/Ti CMNR was increased significantly and its value was calculated to be  $22.2 \text{ m}^3 \cdot \text{m}^{-2} \cdot \text{h}^{-1} \cdot \text{kPa}^{-1}$ . This implied that the effect of Cu/ZnO nanoparticles immobilization in Ti membrane substrate on permeability was smaller than ZIF-8, since the ZIF-8 structure was collapsed during the process of ion-exchange by  $\text{Cu}^{2+}$  and the pores of the membrane can be regenerated.

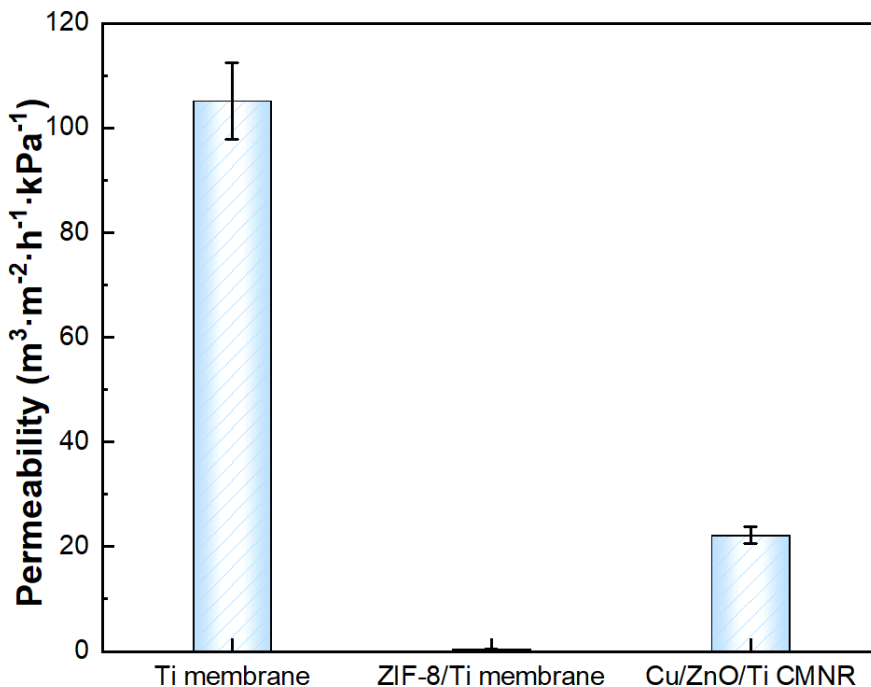


**FIGURE 7** Permeability of Ti membrane substrate, ZIF-8/Ti membrane and Cu/ZnO/Ti CMNR

### 3.2 Catalytic performance of methanol dehydrogenation in CMNR

The conversion efficiencies of methanol dehydrogenation under the reaction temperature 340 , the gas flux  $8 \text{ m}^3 \cdot \text{m}^{-2} \cdot \text{h}^{-1}$  through the membrane, and only one sheet of membrane of thickness 1 mm, are shown in Figure 8. It can be seen that Ti membrane substrate is almost inactive for methanol dehydrogenation. There is a slight increase of conversion efficiency of methanol after the reactant gas permeating through the Cu/Ti membrane and ZnO/Ti membrane. On the contrary, the conversion efficiency of methanol can be increased significantly after the reactant gas permeating through the Cu/ZnO/Ti CMNR, with its value being one order of magnitude higher than the Cu/Ti membrane. The higher conversion efficiency of methanol in the Cu/ZnO/Ti CMNR can be attributed to several factors. Higher Cu immobilization in Cu/ZnO/Ti CMNR could increase contact probability between the catalyst and reactant. Besides, ZnO as Cu carrier can improve the utilization of Cu atom, promote the dispersion of Cu nanoparticles and more catalysis active site can be exposed during the process of methanol crack. Furthermore, Cu and ZnO nanoparticles could synergistic methanol dehydrogenation<sup>34</sup>. It has been reported that the presence of Lewis acid sites on the surface of metal oxides can improve the first step of methanol dehydrogenation-the formation of methoxy<sup>35</sup>. Besides, ZnO also can enhance the spillover of H atoms, which is attributed to the interaction between methanol and O anions of ZnO<sup>36</sup>.

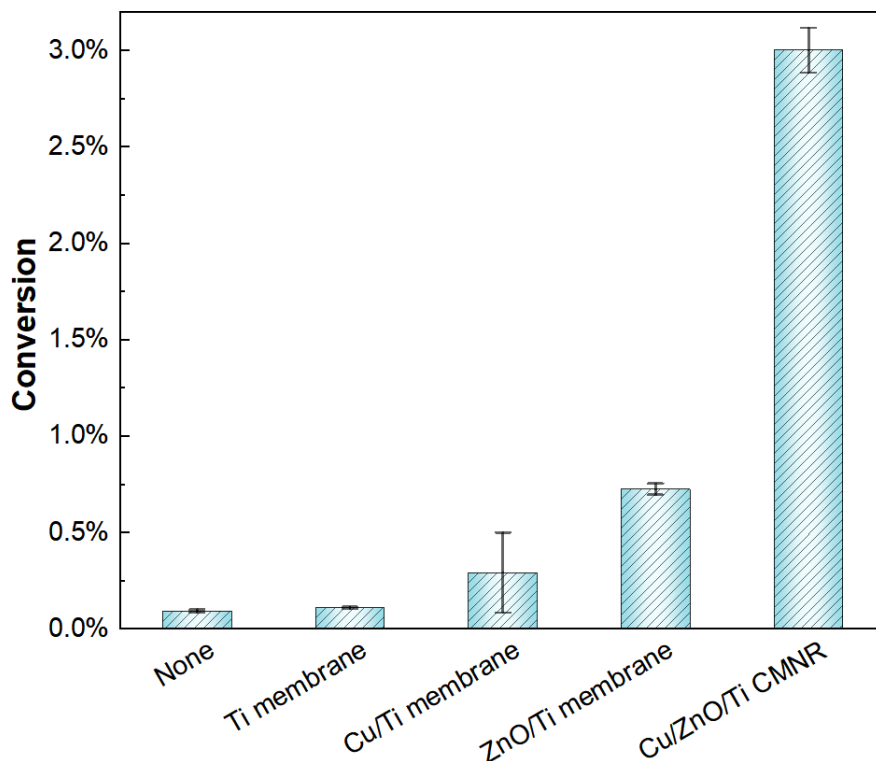


**FIGURE 8** Conversion efficiency of methanol dehydrogenation with different CMNRs. (Reaction temperature 340 , gas flux  $8 \text{ m}^3 \cdot \text{m}^{-2} \cdot \text{h}^{-1}$  through the membrane, one sheet of membrane of thickness 1 mm)

The stability of the Cu/ZnO Ti CMNR was shown in Figure 9. It can be seen that the conversion efficiency of methanol did not decrease significantly and the selectivity of formaldehyde can be kept over 95% after continuous reaction for 18 h, which indicated the Cu/ZnO nanoparticles was not deactivated. In general, carbon deposited produced by side reactions and catalyst sintering caused by local temperature overheating were the common problems for catalyst deactivation during methanol dehydrogenation. In our developed Cu/ZnO/Ti CMNR, the catalyst nanoparticles were immobilized in membrane pores, the uniform distribution and size of membrane pores promote the temperature, methanol concentration and residence time being distributed uniformly. These properties of the CMNR can prevent side reactions and local temperature overheating at the scale of catalytic bed layer. Therefore, high stability of the catalysis performance can be achieved in CMNR for methanol dehydrogenation.

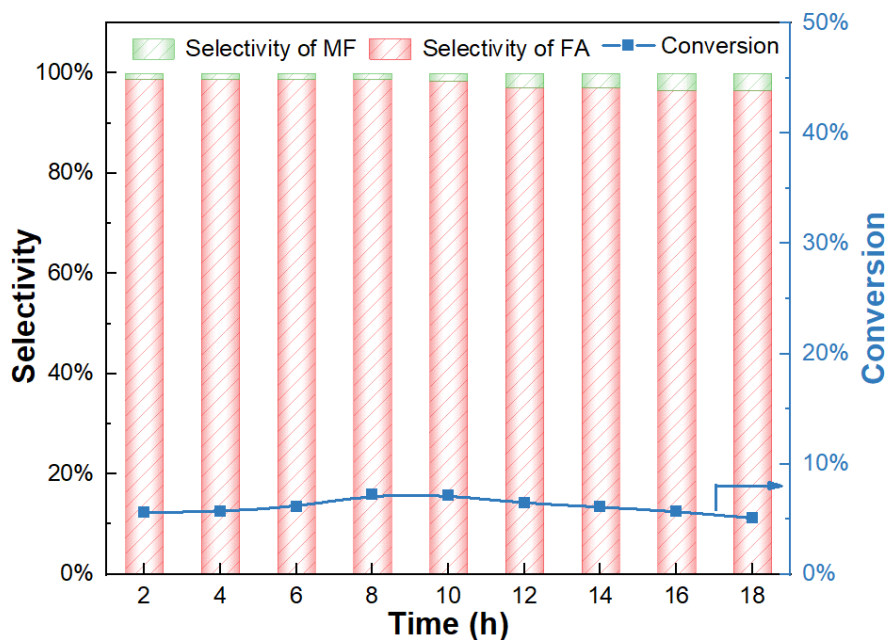


**FIGURE 9** Stability of Cu/ZnO/Ti CMNR in methanol dehydrogenation. (Reaction temperature 360 , gas flux  $8 \text{ m}^3 \cdot \text{m}^{-2} \cdot \text{h}^{-1}$  through the membrane, one sheet of membrane of thickness 1mm)

The catalytic reaction parameters of methanol dehydrogenation with different catalysts (from literatures and this work), including reaction temperature,  $TOF$ ,  $Y_{FA}$  and  $Y_H$ , were illustrated in Table 2. The reported  $TOF$  s ranged from  $0.4 \text{ mmol} \cdot \text{h}^{-1} \cdot \text{g}^{-1}$  to  $130 \text{ mmol} \cdot \text{h}^{-1} \cdot \text{g}^{-1}$ , the  $Y_{FA}$  and  $Y_H$  both ranged from  $0.8 \sim 1.8 \text{ mmol} \cdot \text{h}^{-1} \cdot \text{mm}^{-1}$ , depending on the different reaction temperature and loading amount of catalyst. The  $TOF$ ,  $Y_{FA}$  and  $Y_H$  for methanol dehydrogenation in Cu/ZnO/Ti CMNR developed in this work were much higher than the reported values in literatures. It could be concluded that the Cu/ZnO/Ti CMNR had better catalytic performance for methanol dehydrogenation.

**TABLE 2** Catalytic reaction parameters of methanol dehydrogenation with different catalysts

Catalyst	Reaction Temperature (°C)	Weight of catalyst (mg)	$TOF$ ( $\text{mmol} \cdot \text{h}^{-1} \cdot \text{g}^{-1}$ )	$Y_{FA}$ ( $\text{mmol} \cdot \text{h}^{-1} \cdot \text{mm}^{-1}$ )	$Y_H$ ( $\text{mmol} \cdot \text{h}^{-1} \cdot \text{mm}^{-1}$ )	Ref
CaMoO <sub>4</sub>	400	300	19	-	-	37
Ag-SiO <sub>2</sub> -Al <sub>2</sub> O <sub>3</sub> -ZnO	650	-	-	1.6	1.8	38
MoO <sub>3</sub> /HAP	400	75	55	-	-	39
Ag <sub>2</sub> O/ $\gamma$ -Al <sub>2</sub> O <sub>3</sub>	330	75	71	-	-	40
Ag-SiO <sub>2</sub> -MgO-Al <sub>2</sub> O <sub>3</sub>	650	200	125	0.85	0.85	41
Cu/SiO <sub>2</sub>	280	600	0.44	-	-	42
Cu/HAP	280	600	0.49	-	-	42
Cu/MgO	280	600	0.66	-	-	42
Zn-ZrO <sub>2</sub> /SiO <sub>2</sub>	527	12	66	-	-	43

Catalyst	Reaction Temperature (°C)	Weight of catalyst (mg)	TOF (mmol·h <sup>-1</sup> ·g <sup>-1</sup> )	Y <sub>FA</sub> (mmol·h <sup>-1</sup> ·mm <sup>-1</sup> )	Y <sub>H</sub> (mmol·h <sup>-1</sup> ·mm <sup>-1</sup> )	Ref
Cu/ZnO/Ti CMNR	360	35	183	6.5	6.5	This work

### 3.3 Effect of operation parameters on methanol dehydrogenation

Methanol dehydrogenation was an endothermic process and the increase of reaction temperature could promote the reaction<sup>37</sup>. From Figure 10A, it can be seen that the conversion efficiency of methanol was increased exponentially with reaction temperature. The conversion efficiency of methanol at 360 was two orders of magnitude higher than that at 260. The effect of reaction temperature on the selectivity of products was shown in Figure 10B. The production of formaldehyde and methyl formate performed monotonous tradeoff in the reaction temperature range of 260 and 360, which was consistent with the published reports<sup>44</sup>. The selectivity of formaldehyde can be increased from 10% to 98% with the reaction temperature increased from 260 to 360, and could be kept over than 90%, when the reaction temperature was over 320. This implied that the selectivity of formaldehyde was insensitive to temperature changes, if the reaction temperature was higher. During the process of methanol dehydrogenation for formaldehyde production, the produced formaldehyde would convert into methyl formate through hemiacetal reaction if the formaldehyde couldn't desorb from the active sites in time<sup>45</sup>. In the general fixed bed reactor, the residence time was several seconds<sup>46</sup>. However, the residence time was only 0.2 s with uniform distribution in the developed Cu/ZnO/Ti CMNR. Therefore, the side reaction with methyl formate generation can be inhibited significantly.

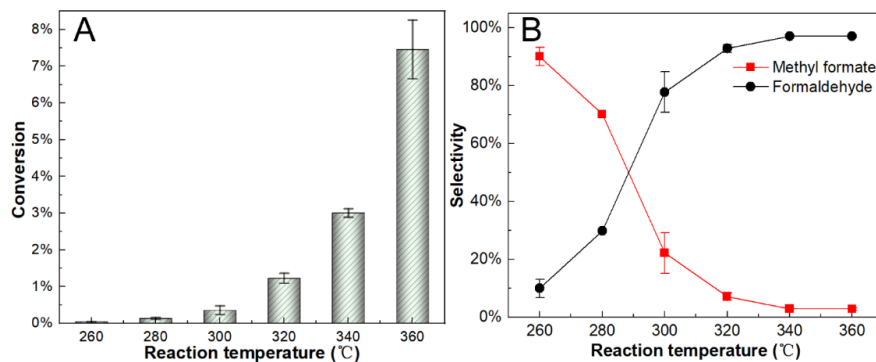


**FIGURE 10** The reaction temperature effect on conversion efficiency of methanol (A) and the selectivity of products (B) of Cu/ZnO/Ti CMNR. (gas flux 8 m<sup>3</sup>·m<sup>-2</sup>·h<sup>-1</sup> through the membrane, one sheet of membrane of thickness 1 mm)

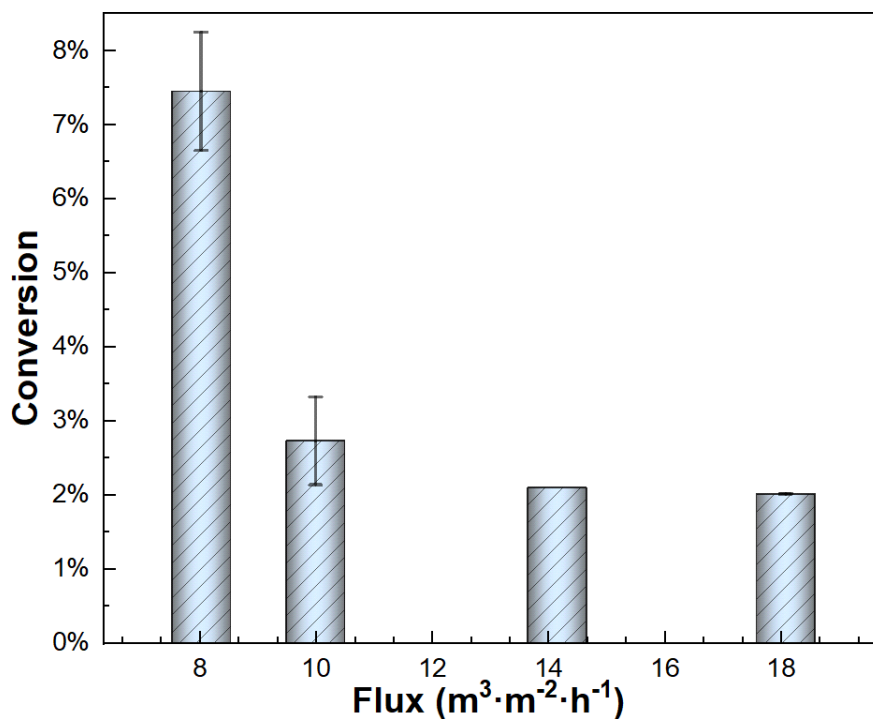


**FIGURE 11** The effect of gas flux on the conversion efficiency of methanol. (Reaction temperature 360 , one sheet of membrane of thickness 1 mm)

The effect of gas flux through the membrane on conversion efficiency of methanol was shown in Figure 11. It could be seen that the conversion efficiency of methanol was decreased from 7.5% to 2.0% with the gas flux through the membrane was increased from 8  $\text{m}^3 \cdot \text{m}^{-2} \cdot \text{h}^{-1}$  to 18  $\text{m}^3 \cdot \text{m}^{-2} \cdot \text{h}^{-1}$  since the reaction residence time during methanol dehydrogenation was decreased. In addition, the gas flux was changed by adjusting the nitrogen flow rate and higher gas flux with higher nitrogen flowrate would cause the decrease of the methanol concentration. It can be calculated that the concentration of the methanol vapor was decreased from 76% to 37% with the gas flux increased from 8  $\text{m}^3 \cdot \text{m}^{-2} \cdot \text{h}^{-1}$  to 18  $\text{m}^3 \cdot \text{m}^{-2} \cdot \text{h}^{-1}$ . Lower gas flux can promote methanol conversion but leads to lower equipment unitization.

In order to obtain high conversion efficiency of methanol under the condition of higher gas flux, two or three sheets of Cu/ZnO/Ti CMNRs were set up in series for methanol dehydrogenation. As shown in Figure 12, it can be seen that the increasing sheets of membrane resulted in an increase of the conversion efficiency of methanol. Moreover, the conversion efficiency of methanol increased asymptotically and reached a maximum value of 18.5% when three sheets of CMNR applied, which produced logically a pressure drop increase from 2.7 kPa to 6.8 kPa. It can be deduced that higher conversion efficiency of methanol can be expected if more membranes are packed in series. Based upon the current experiments, the preliminary simulation could be proposed: if 25 membranes (packing thickness 25 mm) applied, the conversion efficiency of methanol can up to 80% with the gas pressure drop 58 kPa; if Cu/ZnO/Ti CMNRs increased 70 sheets (packing thickness 70mm), the conversion efficiency of methanol would be expected to over 99% with the gas pressure drop 162 kPa. Compared to general fixed bed reactors (conversion efficiency, bed height, pressure drop), the developed here CMNRs would be of excellent performance.

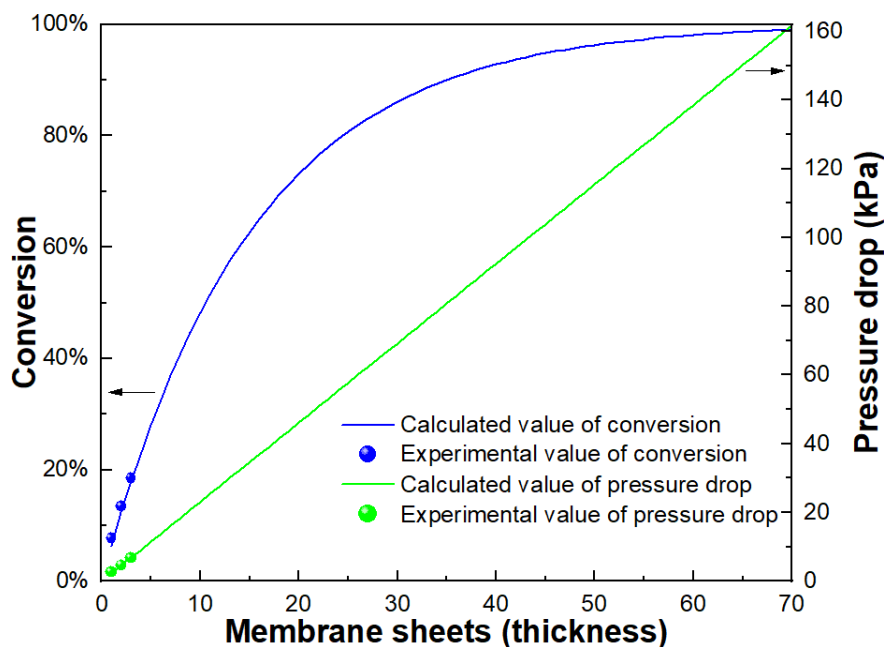


**FIGURE 12** The conversion efficiency of methanol and the pressure drop with increasing membrane sheets (thickness). (Reaction temperature 360 , gas flux  $8 \text{ m}^3 \cdot \text{m}^{-2} \cdot \text{h}^{-1}$  through the membrane)

#### 4 Conclusion

In this work, Cu/ZnO nanoparticles were *in situ* immobilized in the pores of Ti membrane substrate by flowing synthesis with a Cu/ZnO/Ti CMNR fabricated. The characterized results of XRD, XPS, TGA, ICP, SEM and TEM proved the Cu/ZnO nanoparticles were immobilized in the membrane pores and distributed uniformly along the thickness direction of membrane. The developed Cu/ZnO/Ti CMNR was used for the methanol dehydrogenation to anhydrous formaldehyde, and it performed good stability with higher *TOF* and yield. The higher conversion efficiency of methanol and the higher selectivity of formaldehyde can be achieved by increasing the reaction temperature. The conversion efficiency of methanol can also be improved by decreasing the gas flux through the CMNR. Furthermore, the expected high conversion efficiency of methanol can be achieved if more sheets of CMNRs are set up in serials. The CMNR for methanol dehydrogenation would be expected excellent performance over general fixed bed reactor with particulate catalyst.

#### Associated content

The following files are available.

#### Author contributions

Yilin Wang performs experiments, data analysis, figures plotting, and manuscript writing with input from all coauthors; Senqing Fan leads the experiments design, data analysis and contributes to manuscript writing, and is the project administration and leads the whole project; Zeyi Xiao leads the supervision and takes part in the discussion of the project; Other coauthors contribute equally to this work on helping experiment and analysis.

#### Competing interests statement

Declarations of interest: none

#### Acknowledgments

The present work was supported by the National Natural Science Foundation of China (No. 21808144) and the Fundamental Research Funds for the Central Universities (No. 20822041B4013).

## References

1. Millar GJ, Collins M. Industrial Production of Formaldehyde Using Polycrystalline Silver Catalyst. *Ind Eng Chem Res.* 2017; 56(33): 9247-9265, doi:10.1021/acs.iecr.7b02388.
2. Pilato L. *Phenolic Resins: A Century of Progress*. (Berlin, Heidelberg: Springer Berlin Heidelberg, 2010).
3. Li H-J, Lausche AC, Peterson AA, et al. Using microkinetic analysis to search for novel anhydrous formaldehyde production catalysts. *Surf Sci.* 2015; 641(105-111), doi:<https://doi.org/10.1016/j.susc.2015.04.028>.
4. Usachev NY, Krukovskii I, Kanaev SJPC. The nonoxidative methanol dehydrogenation to formaldehyde (A review). 2004; 44(6): 379-394.
5. Zarei M, Davarpanah A, Mokhtarian N, Farahbod FJES, Part A: Recovery, Utilization,, Effects E. Integrated feasibility experimental investigation of hydrodynamic, geometrical and, operational characterization of methanol conversion to formaldehyde. 2020; 42(1): 89-103.
6. Sosna B, Korup O, Horn R. Probing local diffusion and reaction in a porous catalyst pellet. *J Catal.* 2020; 381(285-294, doi:<https://doi.org/10.1016/j.jcat.2019.11.005>.
7. Ajmera SK, Losey MW, Jensen KF, Schmidt MA. Microfabricated packed-bed reactor for phosgene synthesis. *AIChE J.* 2001; 47(7): 1639-1647, doi:<https://doi.org/10.1002/aic.690470716>.
8. Ajmera SK, Delattre C, Schmidt MA, Jensen KF. Microfabricated Differential Reactor for Heterogeneous Gas Phase Catalyst Testing. *J Catal.* 2002; 209(2): 401-412, doi:10.1006/jcat.2002.3584.
9. Wehinger GD, Eppinger T, Kraume M. Evaluating Catalytic Fixed-Bed Reactors for Dry Reforming of Methane with Detailed CFD. *Chem Ing Tech.* 2015; 87(6): 734-745, doi:<https://doi.org/10.1002/cite.201400153>.
10. Su S, Zaza P, Renken AJCE, Engineering-Biotechnology TICPEP. Catalytic dehydrogenation of methanol to water-free formaldehyde. 1994; 17(1): 34-40.
11. Miao J, Lu J, Jiang H, et al. Continuous and complete conversion of high concentration p-nitrophenol in a flow-through membrane reactor. *AIChE J.* 2019; 65(9): e16692, doi:<https://doi.org/10.1002/aic.16692>.
12. Fang X, Li J, Ren B, et al. Polymeric ultrafiltration membrane with in situ formed nano-silver within the inner pores for simultaneous separation and catalysis. *J Membr Sci.* 2019; 579(190-198, doi:<https://doi.org/10.1016/j.memsci.2019.02.073>.
13. Gu Y, Bacchin P, Lahitte J-F, et al. Catalytic membrane reactor for Suzuki-Miyaura C-C cross-coupling: Explanation for its high efficiency via modeling. *AIChE J.* 2017; 63(2): 698-704, doi:<https://doi.org/10.1002/aic.15379>.
14. Peela NR, Mubayi A, Kunzru D. Washcoating of  $\gamma$ -alumina on stainless steel microchannels. *Catal Today.* 2009; 147(S17-S23, doi:<https://doi.org/10.1016/j.cattod.2009.07.026>.
15. Zhang X, Zhong L, Zeng G, et al. Process intensification of honeycomb fractal micro-reactor for the direct production of lower olefins from syngas. *Chem Eng J.* 2018; 351(12-21, doi:<https://doi.org/10.1016/j.cej.2018.06.078>.
16. Chen Y, Mai Z, Fan S, et al. Synergistic enhanced catalysis of micro-reactor with nano MnO<sub>2</sub>/ZIF-8 immobilized in membrane pores by flowing synthesis. *J Membr Sci.* 2021; 628(119233, doi:<https://doi.org/10.1016/j.memsci.2021.119233>.
17. Chen Y, Fan S, Qiu B, et al. Enhanced Catalytic Performance of a Membrane Microreactor by Immobilizing ZIF-8-Derived Nano-Ag via Ion Exchange. *Ind Eng Chem Res.* 2020; 59(44): 19553-19563, doi:10.1021/acs.iecr.0c03707.

18. Qin Y, Jian S, Bai K, et al. Catalytic Membrane Reactor of Nano (Ag+ZIF-8)@Poly(tetrafluoroethylene) Built by Deep-Permeation Synthesis Fabrication. *Ind Eng Chem Res.* 2020; 59(21): 9890-9899, doi:10.1021/acs.iecr.0c00862.
19. Qiu B, Fan S, Wang Y, et al. Catalytic membrane micro-reactor with nano ZIF-8 immobilized in membrane pores for enhanced Knoevenagel reaction of Benzaldehyde and Ethyl cyanoacetate. *Chem Eng J.*2020; 400(125910, doi:<https://doi.org/10.1016/j.cej.2020.125910>.
20. Qiu B, Fan S, Chen Y, et al. Micromembrane absorber with deep-permeation nanostructure assembled by flowing synthesis. *AIChE J.* 2021; 67(8): e17272, doi:<https://doi.org/10.1002/aic.17272>.
21. Seto H, Yoneda T, Morii T, et al. Membrane reactor immobilized with palladium-loaded polymer nanogel for continuous-flow Suzuki coupling reaction. *AIChE J.* 2015; 61(2): 582-589, doi:<https://doi.org/10.1002/aic.14653>.
22. Hoyt RA, Montemore MM, Sykes ECH, Kaxiras E. Anhydrous Methanol and Ethanol Dehydrogenation at Cu(111) Step Edges. *J Phys Chem A.*2018; 122(38): 21952-21962, doi:10.1021/acs.jpcc.8b06730.
23. Hsiao TC, Lin SD. Effect of co-feed species on methanol conversion over Cu/ZnO/Al<sub>2</sub>O<sub>3</sub> and its possible mechanism. *J Mol Catal A: Chem.* 2007; 277(1): 137-144, doi:<https://doi.org/10.1016/j.molcata.2007.07.035>.
24. Manzoli M, Chiorino A, Boccuzzi F. Decomposition and combined reforming of methanol to hydrogen: a FTIR and QMS study on Cu and Au catalysts supported on ZnO and TiO<sub>2</sub>. *Appl Catal B.* 2005; 57(3): 201-209, doi:<https://doi.org/10.1016/j.apcatb.2004.11.002>.
25. Wang N, Liu T, Shen H, et al. Ceramic tubular MOF hybrid membrane fabricated through in situ layer-by-layer self-assembly for nanofiltration. 2016; 62(2): 538-546.
26. Pokhrel J, Bhorla N, Anastasiou S, et al. CO<sub>2</sub> adsorption behavior of amine-functionalized ZIF-8, graphene oxide, and ZIF-8/graphene oxide composites under dry and wet conditions. *Microporous Mesoporous Mater.* 2018; 267(53-67, doi:<https://doi.org/10.1016/j.micromeso.2018.03.012>.
27. Zhang Y, Xie Z, Wang Z, et al. Unveiling the adsorption mechanism of zeolitic imidazolate framework-8 with high efficiency for removal of copper ions from aqueous solutions. *Dalton Trans.* 2016; 45(32): 12653-12660, doi:10.1039/C6DT01827K.
28. Zhou L, Li N, Owens G, Chen Z. Simultaneous removal of mixed contaminants, copper and norfloxacin, from aqueous solution by ZIF-8. *Chem Eng J.* 2019; 362(628-637, doi:<https://doi.org/10.1016/j.cej.2019.01.068>.
29. Zhang L, Hu YHJTJoPCC. Strong effects of higher-valent cations on the structure of the zeolitic Zn (2-methylimidazole) 2 framework (ZIF-8). 2011; 115(16): 7967-7971.
30. Sun S, Yang Z, Cao J, Wang Y, Xiong W. Copper-doped ZIF-8 with high adsorption performance for removal of tetracycline from aqueous solution. *J Solid State Chem.* 2020; 285(121219, doi:<https://doi.org/10.1016/j.jssc.2020.121219>.
31. Kishor R, Ghoshal AK. APTES grafted ordered mesoporous silica KIT-6 for CO<sub>2</sub> adsorption. *Chem Eng J.* 2015; 262(882-890, doi:<https://doi.org/10.1016/j.cej.2014.10.039>.
32. Zhang L, Yang X, Jiang B, et al. Superhydrophilic and underwater superoleophobic Ti foam with robust nanoarray structures of TiO<sub>2</sub> for effective oil-in-water emulsion separation. *Sep Purif Technol.*2020; 252(117437, doi:<https://doi.org/10.1016/j.seppur.2020.117437>.
33. Xu K, Zhan C, Zhao W, et al. Tunable resistance of MOFs films via an anion exchange strategy for advanced gas sensing. *J Hazard Mater.*2021; 416(125906, doi:<https://doi.org/10.1016/j.jhazmat.2021.125906>.

34. Klier K. Structure and function of real catalysts. *Appl Surf Sci.* 1984; 19(1): 267-297, doi:[https://doi.org/10.1016/0378-5963\(84\)90066-7](https://doi.org/10.1016/0378-5963(84)90066-7).
35. McInroy AR, Lundie DT, Winfield JM, et al. An infrared and inelastic neutron scattering spectroscopic investigation on the interaction of  $\eta$ -alumina and methanol. 2005; 7(16): 3093-3101.
36. Yong ST, Ooi CW, Chai SP, Wu XS. Review of methanol reforming-Cu-based catalysts, surface reaction mechanisms, and reaction schemes. *Int J Hydrog Energy.* 2013; 38(22): 9541-9552, doi:<https://doi.org/10.1016/j.ijhydene.2013.03.023>.
37. Said AE-AA, Goda MN. Superior catalytic performance of CaMoO<sub>4</sub> catalyst in direct dehydrogenation of methanol into anhydrous formaldehyde. *Chem Phys Lett.* 2018; 703(44-51, doi:10.1016/j.cplett.2018.05.009.
38. Ren L-P, Dai W-L, Yang X-L, et al. Novel highly active Ag-SiO<sub>2</sub>-Al<sub>2</sub>O<sub>3</sub>-ZnO catalyst for the production of anhydrous HCHO from direct dehydrogenation of CH<sub>3</sub>OH. *Appl Catal A.* 2004; 273(1): 83-88, doi:<https://doi.org/10.1016/j.apcata.2004.06.015>.
39. Said AE-AA, El-Wahab MMMA, Alian AM. Selective Oxidation of Methanol to Formaldehyde Over Active Molybdenum Oxide Supported on Hydroxyapatite Catalysts. *Catal Letters.* 2016; 146(1): 82-90, doi:10.1007/s10562-015-1624-2.
40. Said AE-AA, El-Aal MA. Direct dehydrogenation of methanol to anhydrous formaldehyde over Ag<sub>2</sub>O/ $\gamma$ -Al<sub>2</sub>O<sub>3</sub> nanocatalysts at relatively low temperature. *Res Chem Intermed.* 2017; 43(5): 3205-3217, doi:10.1007/s11164-016-2820-4.
41. Ren L-p, Dai W-l, Cao Y, Li H, Fan K. First observation of highly efficient dehydrogenation of methanol to anhydrous formaldehyde over novel Ag-SiO<sub>2</sub>-MgO-Al<sub>2</sub>O<sub>3</sub> catalyst. *ChemComm.* 2003; 3(24): 3030-3031, doi:10.1039/b310316a.
42. Lu Z, Gao D, Yin H, Wang A, Liu S. Methanol dehydrogenation to methyl formate catalyzed by SiO<sub>2</sub>, hydroxyapatite-, and MgO-supported copper catalysts and reaction kinetics. *J Ind Eng Chem.* 2015; 31(301-308, doi:<https://doi.org/10.1016/j.jiec.2015.07.002>.
43. ZHANG Y, CUI Z-q, YAN S-h, LIU J-w, SHEN J-fJNGCI. Nonoxidative methanol dehydrogenation to anhydrous formaldehyde over Zn-ZrO<sub>2</sub>/SiO<sub>2</sub> catalyst. 2011; 1(
44. Zhang R, Sun Y, Peng S. In situ FTIR studies of methanol adsorption and dehydrogenation over Cu/SiO<sub>2</sub> catalyst. *Fuel* 2002; 81(11): 1619-1624, doi:[https://doi.org/10.1016/S0016-2361\(02\)00085-6](https://doi.org/10.1016/S0016-2361(02)00085-6).
45. Yang H, Chen Y, Cui X, et al. A Highly Stable Copper-Based Catalyst for Clarifying the Catalytic Roles of Cu<sup>0</sup> and Cu<sup>+</sup> Species in Methanol Dehydrogenation. *Angew Chem Int Ed.* 2018; 57(7): 1836-1840, doi:10.1002/anie.201710605.
46. Minyukova TP, Simentsova II, Khasin AV, et al. Dehydrogenation of methanol over copper-containing catalysts. *Appl Catal A.* 2002; 237(1): 171-180, doi:[https://doi.org/10.1016/S0926-860X\(02\)00328-9](https://doi.org/10.1016/S0926-860X(02)00328-9).

#### Hosted file

Table.docx available at <https://authorea.com/users/375918/articles/711377-catalytic-membrane-nano-reactor-with-cu-zno-in-situ-immobilized-in-membrane-pores-for-methanol-dehydrogenation>

